PERGAMON

Chemical Engineering Science 56 (2001) 6635–6649

Chemical Engineering Science

www.elsevier.com/locate/ces

# Integrated experimental and computational approach to simulation of flow in a stirred tank

H. S. Yoon[a], K. V. Sharp[b], D. F. Hill[c], R. J. Adrian[b], S. Balachandar[b,*], M. Y. Ha[a], K. Kar[d]

[a] *School of Mechanical Engineering, San 30 Chang Jeon Dong, Pusan National University, South Korea*
[b] *Department of Theoretical & Applied Mechanics, 216 Talbot Lab, University of Illinois, Urbana, IL 61801, USA*
[c] *Department of Civil & Environmental Engineering, 212 Sackett Building, Pennsylvania State University, University Park, PA 16802, USA*
[d] *The Dow Chemical Company, 1776 Dow Center, Midland, MI, 48674, USA*

Received 29 February 2000; received in revised form 22 February 2001; accepted 23 March 2001

**Abstract**

The stirred tank reactor is one of the most commonly used devices in industry for achieving mixing and reaction. We consider a combined experimental/computational approach for the simulation of flow inside a stirred tank. Two sets of experiments are performed to measure the velocity field in the neighborhood of the impeller. The first set of PIV measurements is on six different $r$–$z$ planes phase locked at $0^\circ$, $10^\circ$, $20^\circ$, $30^\circ$, $40^\circ$ and $50^\circ$ to the blade location. The second set of PIV measurements is on a curved $\theta$–$z$ plane whose radial location is just outside the impeller blade tip radius. Measurements indicate that the impeller-induced flow is dominated by three flow components: a circumferential flow, a tangential jet and pairs of tip vortices. A simple theoretical model is developed for each flow component and their superposition is observed to provide a good description of the impeller-induced flow. The theoretical model is used as a velocity boundary condition for numerical simulation. The impeller-induced boundary condition is fully three dimensional, an important aspect that significantly enriches the mathematical representation of the primary source of motion. The results of two- and three-dimensional simulations are compared with measurements in the interior of the tank. 

*Keywords:* Rushton turbine; Turbulence; Simulation; Mixing; Fluid mechanics; Particle image velocimetry

## 1. Introduction

A stirred tank reactor is one of the most commonly used devices in industry for mixing. Even a simple stirred tank is geometrically complex and under most operating conditions the flow is fully turbulent. The flow is often turbulent over the entire tank; the spatio-temporal complexity of the flow is not limited to the vicinity of the impellers (Rao & Brodkey, 1972). As a result, prediction of flow and mixing in a stirred tank is challenging.

One of the fundamental challenges is to transfer the process technology from the laboratory-scale experiments of a few liters to production-scale stirred tanks of several thousand liters. For lack of a reliable approach to guide the scale-up process, the design of a production-scale stirred tank often evolves through a number of intermediate stages involving laboratory experiments and pilot plants. This time consuming and expensive step-by-step scale-up process is currently necessary to build confidence in the final product. Without further advances, the design of stirred tank reactors will continue to contain uncertainties that can be removed only by recourse to expensive experimental verification and pilot plants.

Development of a reliable computational approach for the design of stirred tank reactors faces an important challenge: incorporation of the effects of the impellers. There have been recent attempts at computing the detailed flow around the impellers using moving/deforming grids and sliding meshes (Luo, Gosman, Issa, Middleton, & Fitzgerald, 1993; Lee, Ng, & Yianneskis, 1996). This approach may be viable at low Reynolds numbers corresponding to slow operating speeds in a small

* Corresponding author. Tel.: +1-217-244-4371; fax: +1-217-244-9090.
*E-mail address:* s-bala@uiuc.edu (S. Balachandar).

0009-2509/01/$ - see front matter 
PII: S0009-2509(01)00315-3

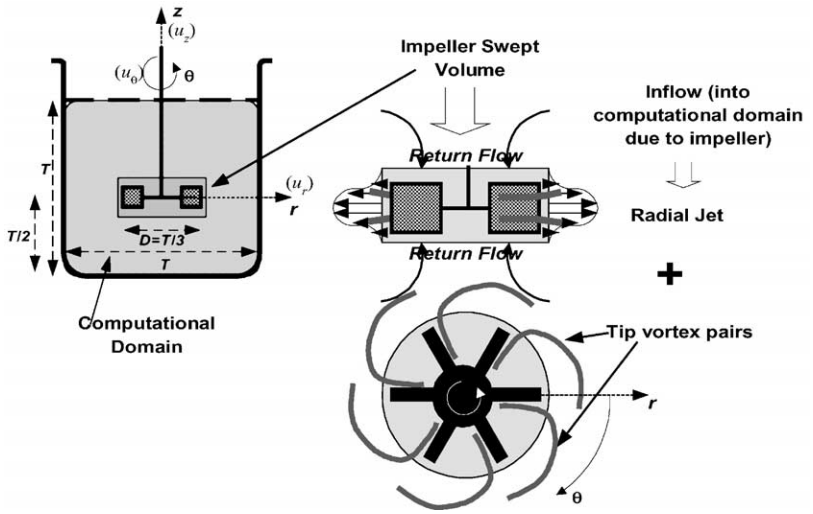


Fig. 1. Schematic of the stirred tank with a typical six-blade Rushton impeller. The plan view shown at the bottom on the right is viewed up from under the tank.

tank. However, at higher Reynolds numbers the flow in the impeller region is quite complex, and the range of length and time scales is so wide as to preclude direct numerical simulation of all these scales. Even large eddy simulation faces a severe challenge in the impeller region. Unlike eddies in the turbulent cascade in the bulk of the tank, in the region close to the impeller the eddies are driven directly by external driving mechanism; they are thus *problem-dependent* and cannot be represented by a universal model.

Instead of a direct computation of the impeller-induced flow, the effect of the impellers can be incorporated into the computations as distributed momentum source (Eggels, 1996; Revstedt, Fuchs, & Tragardh, 1998) or through an approximate aerodynamic theory for the impeller blades (Pericleous & Patel, 1987). In the present work, we address the flow in a stirred tank through a coordinated experimental and computational effort. Particle image velocimetry (PIV) (Sharp, Kim, & Adrian, 1998) and stereoscopic PIV experiments (Hill, Sharp, & Adrian, 2000) are performed to obtain detailed information on the velocity field in the neighborhood of the impeller. Then, computation of the flow is performed outside of the impeller swept volume (see Fig. 1). This procedure generalizes past computations of stirred tank flow, where the average velocity on a pillbox around the impeller obtained from experiment has been used as boundary condition (Ranade, Joshi, & Marathe, 1989; Ju, Mulvahill, & Pike, 1990). In the present work a three-component velocity field is obtained around the impeller region using stereo PIV, thus providing a more realistic complex 3D impeller-induced flow as input for the computations.

Accurate measurement of the velocity field around the impeller swept volume alone is not sufficient for successful interfacing with the computations. A good theoretical model for the impeller-induced flow is required in order to cast the experimental measurement into a meaningful velocity boundary condition. Based on measurements, a simple theoretical description of the impeller-induced flow is developed. Results suggest that the flow induced from the Rushton turbine can be described as a superposition of a circumferential flow, a tangential jet and a pair of tip vortices associated with each impeller blade (see Kolar, Filip, & Curev, 1982, 1984; Kresta & Wood, 1991; Placek & Tavlarides, 1985). The impeller-induced flow is strongly three dimensional (3D), and as a result a complex theoretical description is necessary to capture all the essential features. It must be emphasized that a simple curve-fit or naïve interpolation of the experimental data for application as boundary condition in the computations is futile.

It is important to assess the scaling behavior of the impeller-induced flow with parameters such as the size and rotational speed of the impeller. In practical application, one cannot rely upon performing experiments each time boundary conditions are needed at the impeller swept volume. The computations, after all, are intended to replace the expensive experimental scale-up. The scaling of the velocity boundary condition is complicated by the fact that the impeller-induced flow does not follow a simple scaling with the geometric and operating parameters. A good understanding of each physical mechanism is important in establishing an accurate overall scaling relation. An important advantage of the theoretical description is to simplify the scaling behavior. Each component of the impeller-induced flow (circumferential flow, circular jet and tip vortices) appears to follow a simple scaling law, which is evaluated from a limited set of experiments. However, the individual scaling laws are different for the different components, thus explaining the lack of a simple scaling for the overall impeller-induced flow. Computations are also performed with these

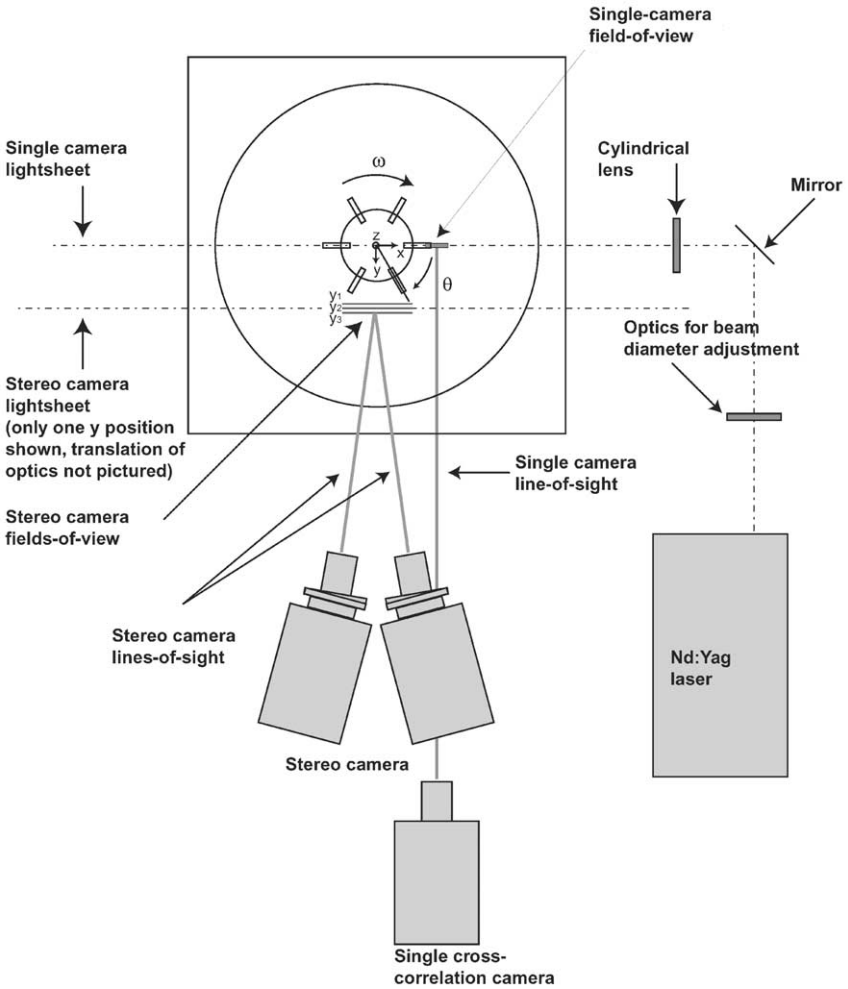


Fig. 2. Top view of the experimental apparatus, including tank, blade, laser lightsheet and measurement plane. Arrangement for both the $r$–$z$ plane and $\theta$–$z$ surface measurements is shown. The velocity field on the curved surface is evaluated using interpolation of the stereo PIV data obtained on three $x$–$z$ planes shown in the figure, at distances 22.94, 25.44 and 26.94 mm from the tank centerline.

boundary conditions and the results are compared with those from experiments.

## 2. Experimental methodology

A schematic of the stirred tank with a single Rushton turbine having six impeller blades located midway between the top and bottom of the tank is shown in Fig. 1 (turbine diameter $D = 50.8$ mm). This geometry is investigated computationally as well with appropriate boundary conditions on the circular surface of the impeller swept volume obtained from the experiments. Proper data-facing between the two is accomplished with a theoretical model for the impeller-induced flow. To best match the computations to be presented below a nonbaffled tank is used for the present measurements.

The purposes of the present experiments are three fold: first to provide the necessary information for the development of accurate velocity boundary conditions on the circular surface of the impeller swept volume; second to obtain physical insights for modeling the impeller-induced flow in terms of identifiable flow mechanisms; and finally to establish a benchmark for the flow and mixing within the stirred tank against which the computational results can be compared for validation. In order to accomplish these objectives three sets of measurements were taken: (1) two-dimensional (2D) PIV measurements on $r$–$z$ planes phase locked at $0^\circ$, $10^\circ$, $20^\circ$, $30^\circ$, $40^\circ$ and $50^\circ$ with respect to the blades. In this set of measurements the field of view is limited to the near blade region; (2) 2D PIV measurements on $r$–$z$ planes, similar to the first set but with a larger field of view; (3) stereoscopic PIV measurements on the $\theta$–$z$ surface of the impeller swept volume (radius $\approx D/2$) to obtain all three components of velocity on this cylindrical surface (Hill et al., 2000).

Fig. 2 shows the experimental setup for the $r$–$z$ plane measurements. A pulsed Nd : Yag laser is used to

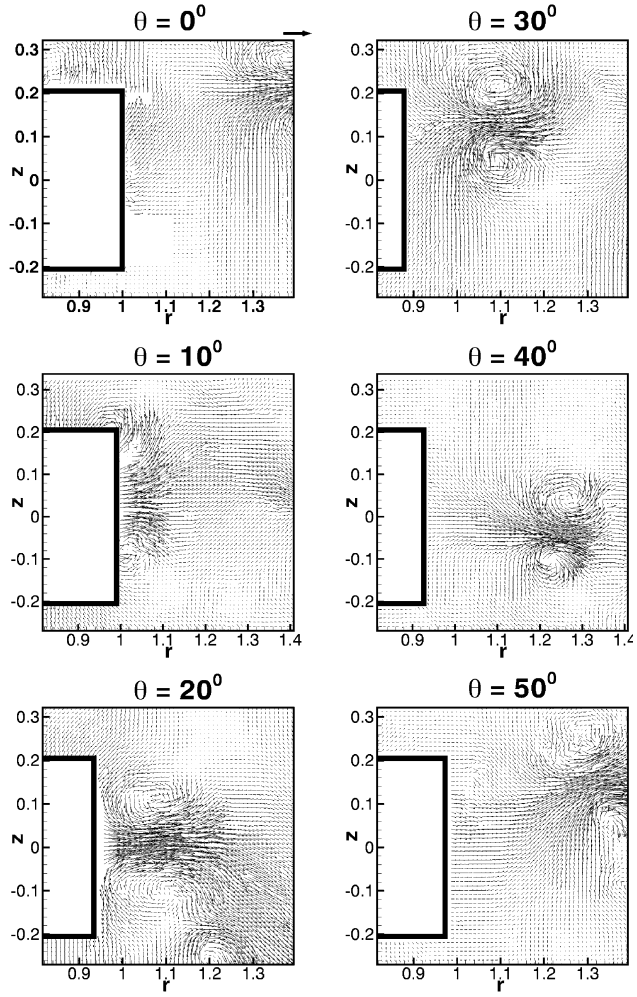


Fig. 3. Typical instantaneous velocity fields measured on the $r$–$z$ planes: (a) $\theta = 0^{\circ}$, (b) $10^{\circ}$, (c) $20^{\circ}$, (d) $30^{\circ}$, (e) $40^{\circ}$ and (f) $50^{\circ}$. The reference vector in frame (a) has magnitude of tip velocity.

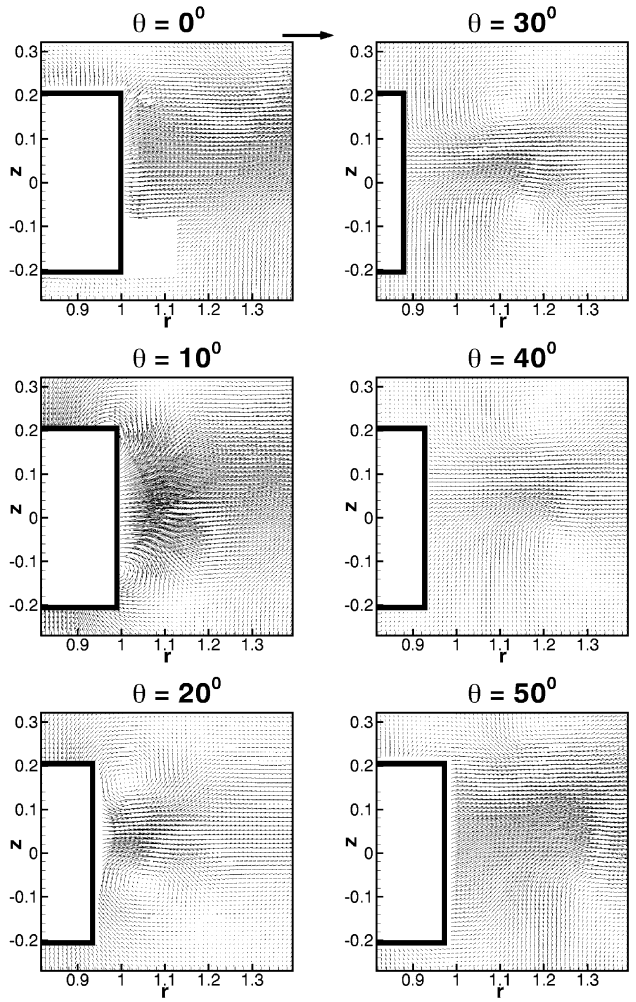


Fig. 4. Phase-averaged velocity fields averaged over 100 instantaneous realizations similar to those shown in Fig. 3: (a) $\theta = 0^{\circ}$, (b) $10^{\circ}$, (c) $20^{\circ}$, (d) $30^{\circ}$, (e) $40^{\circ}$ and (f) $50^{\circ}$. The reference vector in frame (a) has magnitude of tip velocity.

illuminate the particles. The six-blade Rushton turbine has a six-fold symmetry in the azimuthal direction, so only $60^{\circ}$ of phase-locked information is required to define the statistics of the entire flow. Here phase-locked data are acquired in increments of $10^{\circ}$ over the total $60^{\circ}$ sector. One hundred velocity fields are acquired at each phase-locked blade position. Two datasets are obtained with magnifications 0.26 and 0.56.

Samples of instantaneous velocity vector fields at the six different phase-locked locations are shown in Fig. 3 for the smaller field of view. The measurements are taken at an impeller speed of 100 rpm which corresponds to a mixing Reynolds number of $Re = ND^2/v = 4000$, where $N$ is the number of revolutions per second and $v$ is the kinematic viscosity of the fluid. The corresponding phase average taken over 100 realizations is shown in Fig. 4. In this figure and in what follows, all quantities are nondimensional unless specified explicitly in dimensional terms. The tip radius $(D/2)$ is taken as the length scale, the blade tip velocity $(\pi ND)$ is the velocity scale, the time and pressure scales are accordingly defined as $(1/2\pi N)$ and $(\rho[\pi ND]^2)$. In the strict sense there is no symmetry about the $z = 0$ center plane, owing to the free surface at the top. However, for simplicity the computations assume an approximate symmetry in the neighborhood of the impeller. The presence of tip vortices can be observed both in phase-averaged and instantaneous vector plots. The phase-averaged velocities also suggest the presence of a jet with a dominant radial component; this is evident from the vector fields at $\theta = 0^{\circ}$ and $50^{\circ}$, where a strong radial flow can be seen. The flow is quite unsteady with the jet induced by the impeller and the tip vortices meandering up and down the center plane $(z = 0)$.

Fig. 2 also shows the stereoscopic PIV measurement system for the $\theta$–$z$ surface measurement. The measurement on the curved surface is achieved by first obtaining data on three $x$–$z$ planes. More details on the stereoscopic

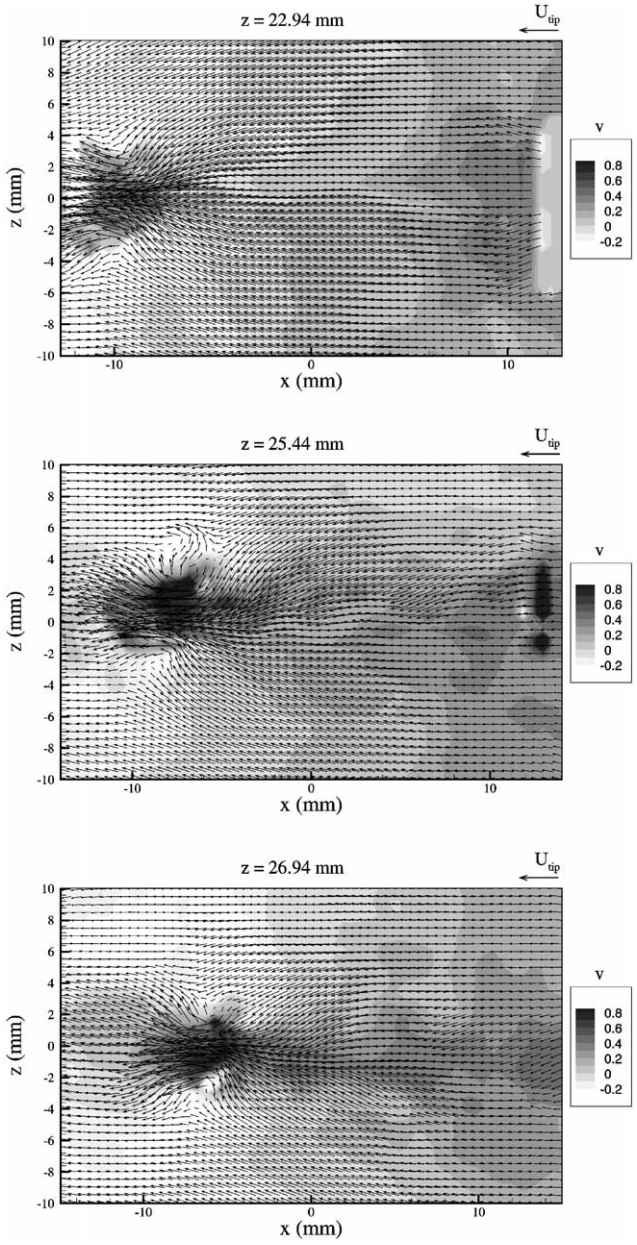


Fig. 5. Sample instantaneous three-dimensional velocity field on the three $x$–$z$ planes for the 100 rpm case. The contours indicate out-of-plane component of velocity. All velocity components have been normalized by the blade tip velocity.

PIV measurement are given in Hill et al. (2000). Experimental results are obtained for three different rotation rates of 50, 100 and 150 rpm corresponding to mixing Reynolds numbers of approximately 2000, 4000 and 6000, which are in the transitional regime. Sample instantaneous velocity fields at the three measurement planes are shown in Fig. 5. One hundred such instantaneous velocity fields are accumulated and averaged at each location, and the resulting data are interpolated onto a cylindrical surface that is enclosed by the data planes. Fig. 6a shows the averaged axial-circumferential velocity field

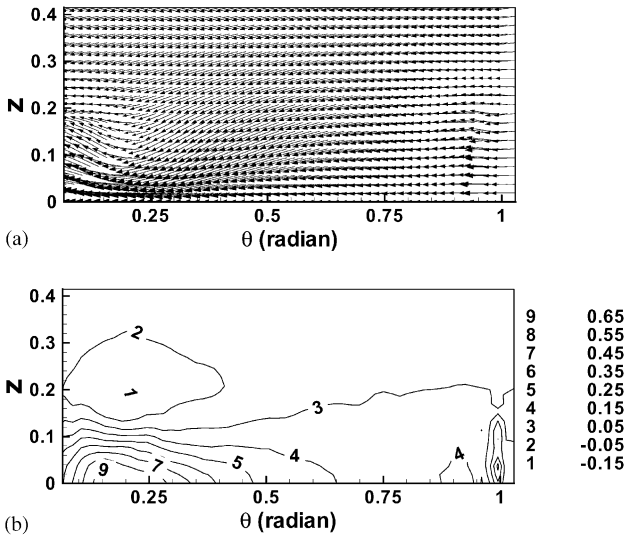


Fig. 6. Phase-averaged three-dimensional velocity field on the curved $\theta$–$z$ surface at ($r \approx 1$) obtained by averaging over 100 realizations: (a) in-plane velocity vector plot and (b) out-of-plane velocity contour. The disturbance seen on the lower right-hand side is due to reflection from the blade.

on the cylindrical surface for 100 rpm. Only a 60° sector is shown. The data are also symmetrized about $z = 0$ and hence only the top half of the swept surface is shown. The radial location of the cylindrical surface is at $R = 26$ mm. The corresponding contours of the out-of-plane radial velocity are shown in Fig. 6b. As shown in Fig. 1 this cylindrical surface cuts through the tip vortex pair and the imprint of the tip vortex pair can be seen in Fig. 6a as the crowding of the vector field around $\theta = 12°$ and $z = 0$. A corresponding increase in the radial velocity can also be observed due to the influence of the tip vortex pair. The flow field in Fig. 6a is dominantly in the negative $\theta$ direction, arising from the impeller-induced circumferential flow (note that the blade is also rotating in the negative $\theta$ direction).

## 3. Theoretical model of impeller-induced flow

The dominant effect of the rotating Rushton impeller is to generate a mean circumferential flow, a jet flow and pairs of tip vortices. In the case of a Rushton turbine the jet flow slowly changes direction from a circumferential direction to a radial direction with increasing distance from the axis of the impeller. Furthermore, the tip vortex pair is on average nearly symmetric. Here we will consider simple theoretical models of these individual components and how the experimental measurement fits the theoretical model.

### 3.1. Tangential jet

The jet flow from a Rushton turbine is traditionally approximated as a radial jet (Schwarz, 1963). However, experimental results suggest that the data can be better approximated as a tangential jet (Nielsen, 1958). Using the results of Nielsen (1958), Desouza and Pike (1972) separated the stirred tank into several regions and used different theoretical models to describe the flow in each region.

The tangential jet is purely circumferential at its virtual source but progressively turns to a radial orientation as radius increases out from the virtual source, due to centrifugal effects (Nielsen, 1958; Desouza & Pike, 1972). This flow can be thought of as resulting from an infinitely thin circular ring of radius $a$, rotating infinitely fast in an unbounded fluid medium, but imparting finite net momentum to the fluid. Standard boundary layer theory can be applied and an approximate self-similar solution can be obtained. In this model the jet has three components of velocity, but they depend only on the radial and axial coordinates. The jet velocity can be expressed as

$$u_{Jq} = U_J\{1 - \tanh^2(\eta)\}, \tag{1}$$

where the centerline velocity of the jet, $U_J$, shows the following behavior with the radial location, $r$:

$$U_J = \frac{A}{r^{1/2}} \frac{1}{(r^2 - a^2)^{1/4}} \tag{2}$$

and the self-similar axial distance, $\eta$, is defined as

$$\eta = \frac{\sigma z}{\sqrt{r^2 - a^2}}. \tag{3}$$

From the above jet velocity the radial and circumferential components of the jet can be obtained in terms of the jet angle, $\theta_J = \cos^{-1}[\sqrt{r^2 - a^2}/r]$, as

$$u_{Jr} = u_{Jq}\cos(\theta_J) \quad \text{and} \quad u_{J\theta} = u_{Jq}\sin(\theta_J). \tag{4}$$

In the above equations $A$ measures the momentum of the jet and $\sigma$ measures the width of the jet (jet thickness parameter). At the virtual origin ($r = a$) the jet is entirely circumferential, and for $r \gg a$ the jet is entirely radial. Owing to entrainment there is an axial component to the circular jet, which can be approximately obtained from the continuity equation as

$$u_{Jz} = U_J \left\{ \frac{z}{(r^2 - a^2)^{1/2}}[1 - \tanh^2(\eta)] - \frac{(2r^2 + a^2)}{2\sigma r^2}\tanh(\eta) \right\}. \tag{5}$$

Eqs. (1)–(5) exactly conserve jet momentum

$$2\pi r \int_{-\infty}^{\infty} u_{Jq}^2 \, \mathrm{d}z = \frac{2\pi r^3}{(r^2 - a^2)} \int_{-\infty}^{\infty} u_{Jr}^2 \, \mathrm{d}z = \text{constant}. \tag{6}$$

In this model the three parameters that control the jet flow are: the virtual origin ($a$), the jet strength ($A$) and the jet width ($\sigma$). Later we will extract the value of these three parameters from experimental data. Other approximations such as turbulent swirling radial-jet model (Kolar et al., 1982, 1984; Kresta & Wood, 1991), are possible. Nevertheless, here we will pursue the tangential jet model, mainly for its simplicity. As will be shown below, the tangential jet model provides an adequate description of the impeller-induced flow for the present purposes.

The velocity field shown in Fig. 6 around the impeller swept volume includes contributions from both the jet and the tip vortex pair. To obtain the parameters associated with the jet from the experimental measurement it is necessary to isolate the contribution of the jet. While the jet component is taken to be independent of the azimuthal direction ($\theta$), the velocity contribution from the tip vortices is strongly dependent on $\theta$. At the surface of the impeller swept volume the center of the tip vortex pair is located at about 12° to the blade location (this assertion will be verified below). For large distances, the influence of the tip vortex decays as inverse distance from the vortex core. Thus, as we move away to $\theta \approx 45^\circ$, the velocity field is dominated by the jet component. Furthermore, on the $\theta$–$z$ plane of the impeller swept volume, the radial component of velocity is dominantly due to the jet and the contributions from the tip vortices and circumferential flow are likely to be minimal. Based on the above arguments the radial velocity in the region $\theta = 40$–$50^\circ$ is dominated by the jet flow and little influenced by the tip vortices. The circumferential, radial and axial velocities obtained from the stereoscopic PIV measurements are shown in Fig. 7 at three different circumferential locations ($\theta = 40^\circ$, 45° and 50°). The circumferential and radial components show little variation confirming that the nearly uniform flow in this region is dominantly due to the jet. The jet parameters, $a$, $A$ and $\sigma$, are determined using a nonlinear optimization procedure by projecting the stereoscopic PIV data in the region $\theta = 40$–$50^\circ$ onto the theoretical model given in Eqs. (1)–(5). The resulting optimal jet parameters in nondimensional terms are: $a = 0.67$, $A = 0.163$ and $\sigma = 5.0$. Fig. 7 also shows the model velocities obtained from Eqs. (1)–(5) using the above values.

A constant lag can be seen in the case of circumferential velocity, which was also observed by Desouza and Pike (1972). Here we associate the difference to a circumferential flow, $u_{C\theta}(r)$, which is considered to be axisymmetric and independent of the axial direction. $u_{C\theta}$ can be considered as an average swirling flow that exists in addition to the tangential jet. Fig. 7 shows that a circumferential flow defined in nondimensional terms as $u_{C\theta} = -0.42$ is able to reproduce the measurement accurately. Thus the circumferential flow component has also been determined from the PIV measurement.

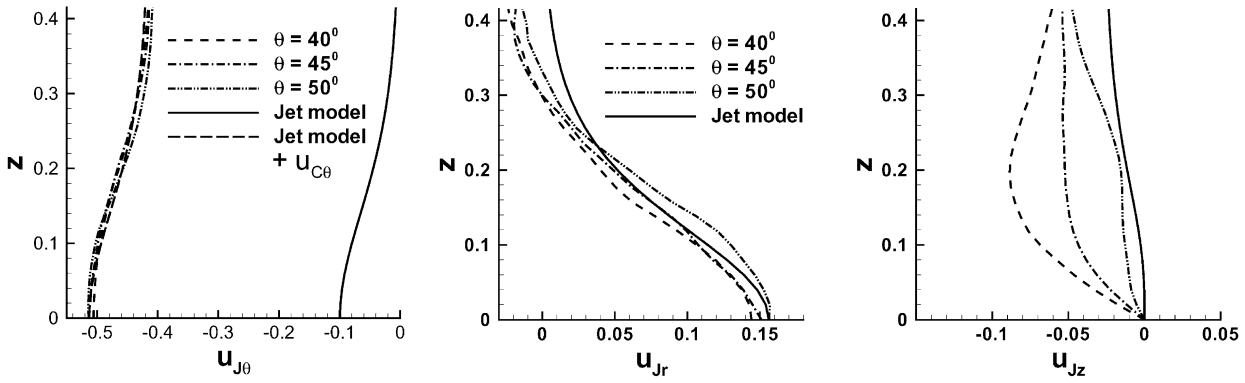


Fig. 7. The (a) circumferential, (b) radial and (c) axial velocities obtained from the stereoscopic PIV measurement at three different circumferential locations: $\theta = 40^{\circ}, 45^{\circ}$ and $50^{\circ}$. Also shown for comparison are the corresponding velocity from the theoretical jet model. In the case of $u_\theta$ profiles with and without the circumferential flow component are shown.

### 3.2. Tip vortices

The tip vortices are generated from the roll-up of the shear layers as flow accelerates around the rotating impellers. Their presence has been suggested by past experimental observations and measurements (Van't Riet & Smith, 1975; Yianneskis, Popiolek, & Whitelaw, 1987; Calabrese & Stoots, 1989). Here we follow a modified version of the procedure introduced by Placek and Tavlarides (1985) for the tip vortex model. As shown in Fig. 1, the trajectory of each tip vortex pair is curved. The tip vortices are characterized by their trajectory (their radial and axial position), their strength, $\Gamma(\theta)$, and size, $\delta(\theta)$, where again $\theta$ measures the angle from the impeller blade in the direction opposite to the blade rotation. First we extract the trajectory of the vortex from the PIV measurements in the $r$–$z$ and $\theta$–$z$ planes. Measurements of the mean velocity field in the $r$–$z$ plane at $\theta = 10^{\circ}$, $20^{\circ}$, $30^{\circ}$, $40^{\circ}$ and $50^{\circ}$, after subtraction of the jet and circumferential flow components, are shown in Fig. 8. The presence of a pair of vortices can be clearly seen after the jet contribution has been removed. With increasing $\theta$ the vortex centers can be observed to move out in $r$ and the axial separation of the vortex pair also slightly increases. Fig. 9a shows the trajectory of the vortex in the $x$–$z$ plane and the circle traced by the tip of the impeller. The corresponding trajectory in the $z$–$\theta$ plane is shown in Fig. 9b. A linear fit through the data

$$r_v(\theta) = 0.86 + 0.47\theta \quad \text{and} \quad z_{v\pm}(\theta) = \pm(0.06 + 0.08\theta) \tag{7}$$

provides an adequate description of the radial and axial location of the center of the tip vortex pair ($z_{v+}$ and $z_{v-}$ correspond to the vortex above and below the center plane at $z = 0$).

For the velocity boundary condition it is of interest to obtain all three components of velocity induced by the tip vortex system at any point **P** along the impeller swept boundary. With a description of the vortex trajectory and strength, the velocity induced at **P** can be expressed as a line integral according to the Biot–Savart law (Saffman, 1992). Considerable simplification can be achieved by assuming that the dominant influence comes from points $\mathbf{Q}_+$ and $\mathbf{Q}_-$ along the top and bottom vortices of the pair where the vortex axis is normal to the line joining **P** and **Q**. For every point **P** a companion pair of points $\mathbf{Q}_+$ and $\mathbf{Q}_-$ along the vortex pair can be identified whose position is given by $(r_v(\theta_Q), \theta_Q, z_{v\pm}(\theta_Q))$. The tip vortices are assumed to be viscous and velocity induced at point **P** is then given by

$$u_{Vs} = -\frac{\Gamma}{2\pi}\left[\frac{z_+}{d_+^2}\left\{1 - \exp\left(-\frac{d_+^2}{\delta^2}\right)\right\} - \frac{z_-}{d_-^2}\left\{1 - \exp\left(-\frac{d_-^2}{\delta^2}\right)\right\}\right], \tag{8a}$$

$$u_{Vz} = -\frac{\Gamma}{2\pi}\left[\frac{r_s}{d_+^2}\left\{1 - \exp\left(-\frac{d_+^2}{\delta^2}\right)\right\} - \frac{r_s}{d_-^2}\left\{1 - \exp\left(-\frac{d_-^2}{\delta^2}\right)\right\}\right], \tag{8b}$$

where $r_s$ measures distance between **P** and **Q** along a plane perpendicular to the tank axis and normal to the vortex trajectory. The total distance from **P** to $\mathbf{Q}_+$ and $\mathbf{Q}_-$ is given by $d_\pm$. Here $\Gamma$ and $\delta$ measure the strength (circulation) and size of the vortices at **Q**. In Eq. (8a) $u_{Vs}$ is the vortex-induced velocity component along the $s$-axis (line joining the projections of **P** and **Q** on the $z = 0$ plane), from which the radial, $u_{Vr}$, and circumferential, $u_{V\theta}$, components can be easily evaluated.

The 2D velocity fields measured on $r$–$z$ planes, after subtraction of the jet component ($\tilde{u}_{Vr}$ and $\tilde{u}_{Vz}$) shown in Fig. 8, are used to compute the vortex strength and size by comparing them with the above theoretical model. In each plane, attention is focused on the region close

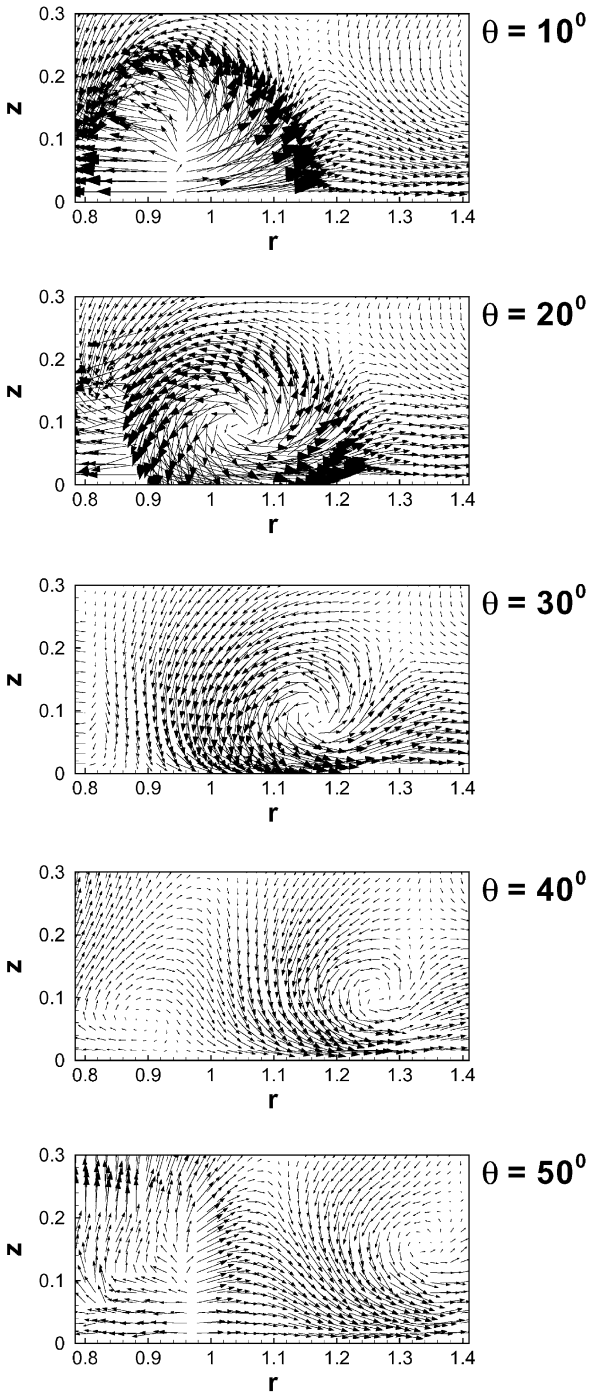


Fig. 8. Experimental measurements of mean velocity field in the $r$–$z$ plane at (a) $\theta = 10^{\circ}$, (b) $20^{\circ}$, (c) $30^{\circ}$, (d) $40^{\circ}$ and (e) $50^{\circ}$, after subtraction of the theoretical jet and circumferential flow components.

to the tip vortices. The amplitude of error between the experimentally measured velocity field and that obtained from the above theoretical model is defined as

$$e(r,z) = [(u_{Vr} - \tilde{u}_{Vr})^2 + (u_{Vz} - \tilde{u}_{Vz})^2]^{1/2}. \quad (9)$$

The optimal values of local $\Gamma$ and $\delta$ are evaluated by minimizing the rms error integrated over a region around

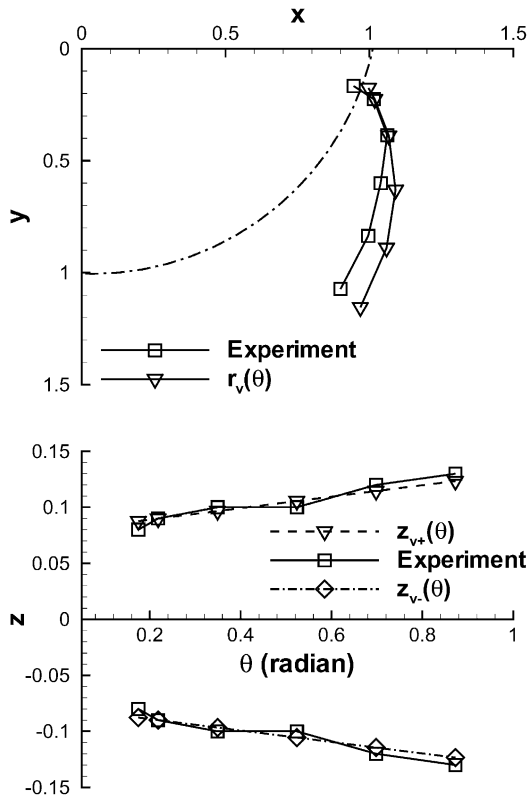


Fig. 9. Trajectory of the tip vortex pair in the $x$–$y$ plane; both experimental measurement and linear fit (Eq. (7)) are shown. Also shown is the circle traced by the blade tip.

the vortex. The variation in $\Gamma$ and $\delta$ measured at $\theta = 10$–$50^{\circ}$ is shown in Fig. 10. A smooth reduction in the vortex strength along its length from its peak value can be observed. The corresponding vortex core size also decreases, possibly due to stretching and possibly due to the fact that the scatter in the instantaneous location of the vortex center increases as the vortex pair moves away from the blade into the tank. Also marked in the figures (as filled circle) are the average values of $\Gamma$ and $\delta$ obtained from a similar error minimization procedure for the stereoscopic PIV measurements on the $z$–$\theta$ plane. This result can be interpreted as an average $\Gamma$ and $\delta$, averaged over the entire length of the vortex pair. Since the vortex pair cuts this $z$–$\theta$ plane around $\theta = 12^{\circ}$, a larger weighting for small $\theta$ and smaller weighting for larger $\theta$ is expected in the average. The resulting $\Gamma_{\text{avg}} = 0.26$ and $\delta_{\text{avg}} = 0.072$ are well within their range measured on individual $\theta$-planes. The measured vortex circulation is the strongest at $\theta = 10^{\circ}$ with $\Gamma = 0.3$ and is very compact with $\delta = 0.088$, which yields a peak nondimensional vortex-induced velocity of $0.1\Gamma/\delta$ for a single vortex, which is about 35% of the blade tip velocity. At $\theta = 50^{\circ}$ the vortex circulation has fallen to $\Gamma = 0.065$ and its size has changed to $\delta = 0.057$; the corresponding peak induced velocity is now only 11% of blade tip velocity.

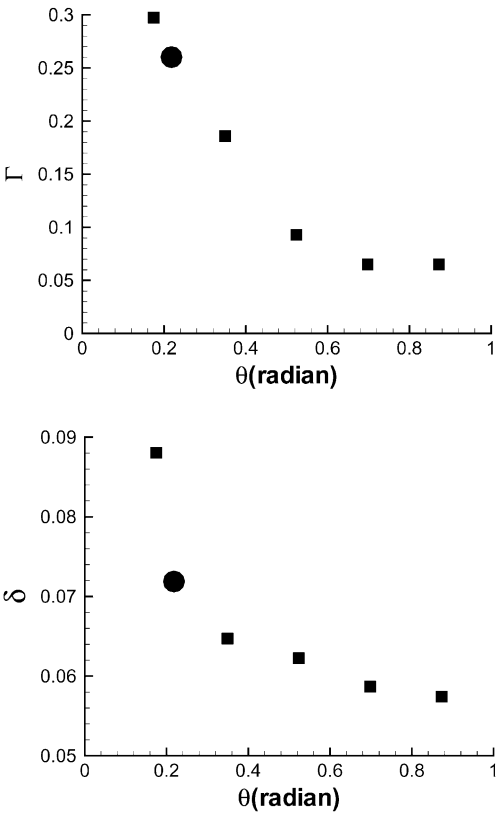


Fig. 10. Variation in tip vortex (a) strength and (b) size with $\theta$. ■: obtained from the $r$–$z$ plane measurements; ●: obtained from the $\theta$–$z$ surface measurement.

### 3.3. Comparison with experiments

The above analytical expressions for the jet and tip vortex flows are valid only in the region close to the impellers; as we move outward the effect of the outer walls of the tank must be accounted for. Nevertheless, the near field of the impeller-induced flow can be expressed as

$$\mathbf{u}_I(r,\theta,z,t) = \mathbf{u}_J(r,z) + \mathbf{u}_V(r,\theta,z,t) + \mathbf{u}_C(r) \qquad (10)$$

where $\mathbf{u}_C$ is the mean circumferential flow. It is important to note that the above model includes all three (radial, circumferential and axial) components of velocity. The impeller-induced flow varies along the circumferential direction as well due to the presence of tip vortices. Inclusion of the tip vortices leads to a time-dependent impeller-induced flow (in the laboratory frame of reference) arising from the rotation of the blades.

The above theoretical model needs to be evaluated by comparing the results with experimental measurements. Comparisons will be made in both the $r$–$z$ and $\theta$–$z$ planes. First, in Fig. 11, radial velocity profile as a function of axial location at $r = 1$ obtained from the analytical model (Eq. (10)) is compared with the experimental measurements at four different azimuthal locations. The model provides a good description of the experimental measurement. The velocity field on the curved surface surrounding the impeller evaluated from the theoretical model is shown in Fig. 12.

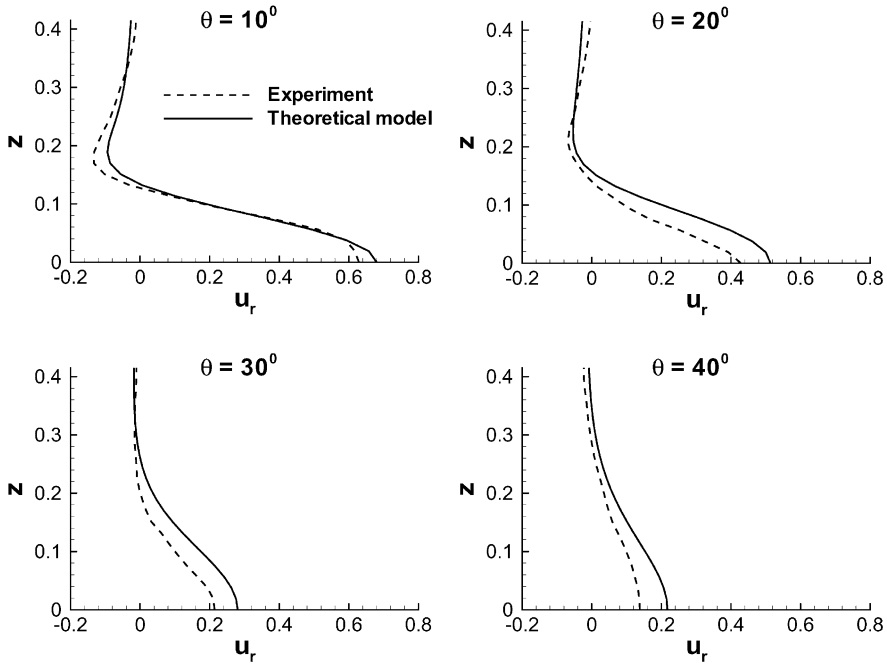


Fig. 11. Radial velocity profile as a function of axial location at $r = 1$ obtained from the theoretical model compared with the corresponding experimental measurements: (a) $\theta = 10^\circ$, (b) $20^\circ$, (c) $30^\circ$ and (d) $40^\circ$.

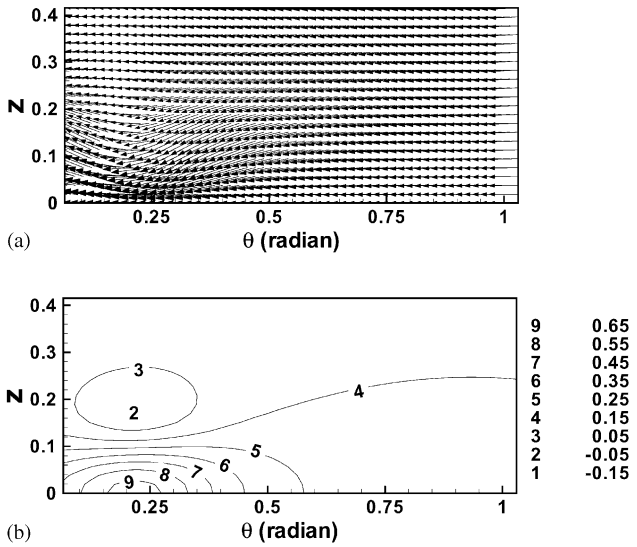


Fig. 12. Same as Fig. 6 for the theoretical model.

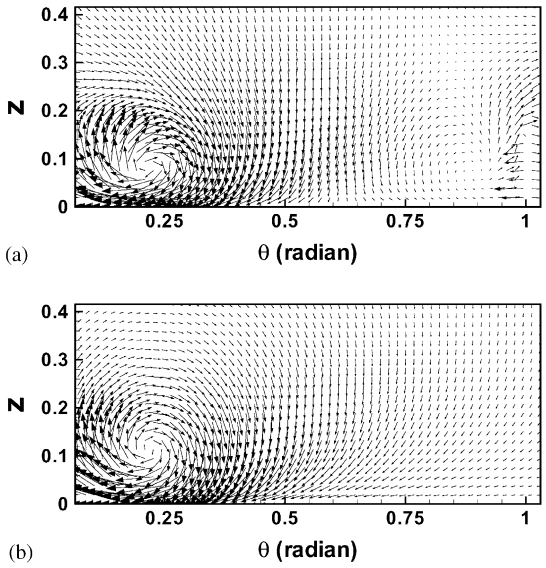


Fig. 13. A closer comparison of the tip vortex field after subtraction of the jet component: (a) experimental measurement and (b) the theoretical model. Noise in the experimental measurement near the lower right hand corner is due to blade reflection.

Both the in-plane velocity vector plot (Fig. 12a) and the out-of-plane velocity contours (Fig. 12b) compare favorably with the corresponding experimental measurements shown in Figs. 6a and 6b. A closer comparison of the tip vortex field is shown in Fig. 13 where the velocity field after subtraction of the jet component is shown for both the experimental measurement and the theoretical model.

It can be argued that good comparison between the experiments and the model is to be expected. After all, the parameters for the model were obtained from the experiments. Nevertheless, the experimental data that are being

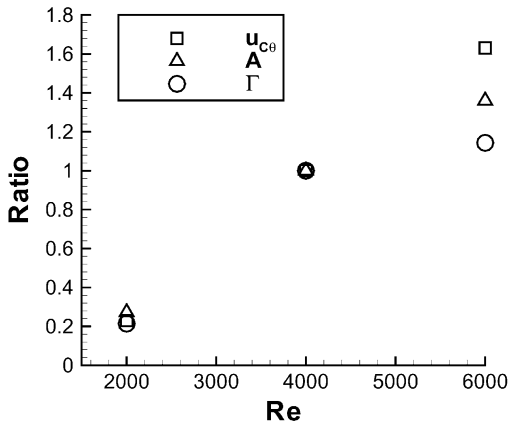


Fig. 14. Scaling of circumferential flow, jet strength ($A$) and circulation of the tip vortex pair ($\Gamma$) with $Re$. All three quantities are plotted as a ratio with respect to their value at the intermediate Reynolds number of 4000 corresponding to 100 rpm.

approximated are complex and fully 3D. All three components of velocity are significant, and they vary in all three coordinate directions. A simple curve fit through the experimental data would not satisfy kinematic constraints and could be futile. A sound theoretically based model is essential to capture the complex variation. Furthermore, the model reduces the prescription of the boundary condition to a few physically meaningful parameters such as amplitudes and width of the jet and the tip vortices. This allows physically meaningful scaling of the impeller-induced flow with impeller size and speed of rotation. The data for 50, 100 and 150 rpm (i.e., $Re = 2000$, 4000 and 6000) can be used to establish the scaling of the three different impeller-induced flow components. Fig. 14 shows variation in circumferential flow, jet strength ($A$) and circulation of the tip vortex pair ($\Gamma$) with $Re$ (all quantities are plotted as a ratio with respect to their value at $Re = 4000$). It appears that the strength of all three components scale similarly from 2000 to 4000, but differently as Reynolds number increases above 4000. Admittedly, the range of Reynolds number considered is very limited; nevertheless it appears that the three different components are likely to scale differently with increasing $Re$. This provides a possible explanation for the complex scaling for the overall impeller-induced flow.

The theoretical model presented above is by no means perfect. Improved models of the jet flow and tip vortices can be sought. Instantaneous PIV realizations clearly reveal that the individual flow components are time dependent. For instance, the impeller-induced jet appears to oscillate up and down about its mean radial trajectory, resulting in a faster axial spreading of the jet flow. Such asymmetry seems to exist between the top and bottom tip vortices as well at any given instance in time. The theoretical framework can be extended to introduce the effect of asymmetry as well.

## 4. Computational approach

We have performed Reynolds-averaged Navier–Stokes simulations of flow inside the stirred tank at $Re = 4000$ using the commercial code FLUENT®. The impeller-induced flow on the surface of the swept volume is used as the input driving mechanism for the flow. The computations are performed in a frame of reference rotating with the impeller. In this rotating frame, the model for the impeller-induced velocity field appears as a steady boundary condition. In the absence of any baffles the statistics are stationary, independent of time, in the rotating frame of reference. Thus a Reynolds-averaged simulation for the time-averaged flow is appropriate. The time-averaged flow has a six-fold symmetry and here we consider only a 60° sector between adjacent impeller blades.

The velocity field shown in Fig. 12, appropriately adjusted for the rotating frame of reference, is applied as the boundary condition at the surface of the impeller swept volume ($r = 1$). The no-slip boundary conditions at the bottom and the outer tank surfaces transform in the rotating frame of reference to surfaces rotating in the opposite direction. For simplicity the top surface is also considered to be no-slip. A symmetry boundary condition is used at $r = 0$.

An important consequence of including the tip vortices in the theoretical model is that the boundary condition is dependent on the azimuthal direction. Thus even in the context of Reynolds-averaged simulation for the time-averaged flow, a 3D simulation within the 60° sector is required. A 3D grid of $40 \times 81 \times 16$ points along the radial, azimuthal and axial directions is used to compute the flow. A nonuniform grid with grid clustering near the impeller region is used in all three directions in order to better resolve the complex flow near the impeller. For comparison a simultaneous 2D Reynolds-averaged simulation is also performed, where the flow is assumed to be independent of the $\theta$-direction. In the 2D simulation, the velocity field shown in Fig. 12 is $\theta$-averaged and applied as the boundary condition for the impeller-induced flow. The geometry and other boundary conditions on the $r$–$z$ plane are the same as in the 3D simulation.

Figs. 15a and b show the velocity vector plot on the $r$–$z$ plane computed from the 3D and the 2D simulations. Both the flows appear to be qualitatively similar with a pair of large vortices that span the entire top and bottom halves of the stirred tank. However, a number of subtle differences can be observed. The centers of the large eddies are located at a radial position of $r \approx 2.2$. In the case of the 2D simulation the center's axial position is farther away from the centerline at $z \approx \pm 0.8$, whereas in the 3D simulation the centers are somewhat closer to the centerline at $z \approx \pm 0.6$. Also, in the case of 3D simulation the impeller-induced jet after hitting the outer wall turns and travels all the way to the top and the bottom of the tank

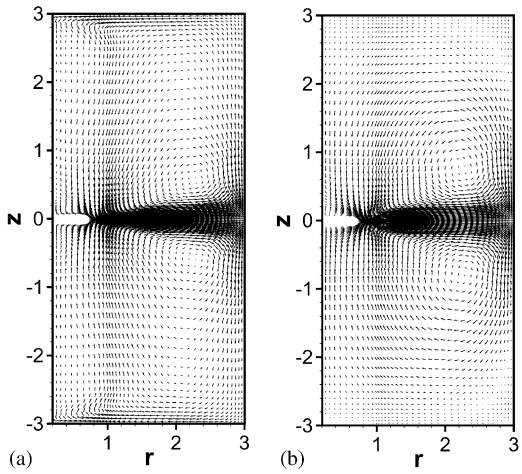


Fig. 15. Velocity vector plot on the $r$–$z$ plane computed from (a) the three-dimensional and (b) the two-dimensional simulations. In the case of the three-dimensional simulation, the $\theta$-averaged flow is plotted.

before returning back to the impeller; thus the pair of eddies cover almost the entire tank. In the case of the 2D simulation the eddies separate from the outer wall before reaching the top and the bottom. As a result, they generate a pair of secondary eddies located in the outer top and bottom corners of the tank, whose direction of rotation is opposite to those of the primary eddies. This difference might have a strong influence on the degree and extent of mixing predicted by the two different simulations.

The width of the impeller-induced jet-like flow increases rapidly from its starting point at $r=1$ in the case of the 2D simulation, whereas in the case of 3D simulation the jet stays focused for a short radial distance (up to about $r \approx 1.25$) before spreading. This difference can be seen clearly in the centerline ($z = 0$) radial velocity profile for both the 2D and 3D simulations (Fig. 16a). The 3D results are averaged along the $\theta$-direction. Also plotted for comparison are the corresponding experimental $\theta$-averaged measurement. In both the 3D simulation and in the experimental measurements the azimuthal-averaged radial velocity can be seen to first increase with $r$ before decaying like a jet. This increase is due to the influence of tip vortices. The tip vortices' influence is confined to their neighborhood, thus resulting in an increase in radial velocity immediately following the tip radius ($r=1$). Farther away the influence of the jet dominates, resulting in the decay of the radial velocity. The predicted maximum radial velocity lies farther out from the tip than the experimental maximum as previously been observed in time-dependent 3D large-eddy simulations (Eggels, 1996; Revstedt et al., 1998). On the other hand, most Reynolds-averaged simulations have failed to accurately capture the presence of the tip vortices and without their influence the radial velocity decays monotonically immediately from its maximum value at the blade tip. Note that with the improved

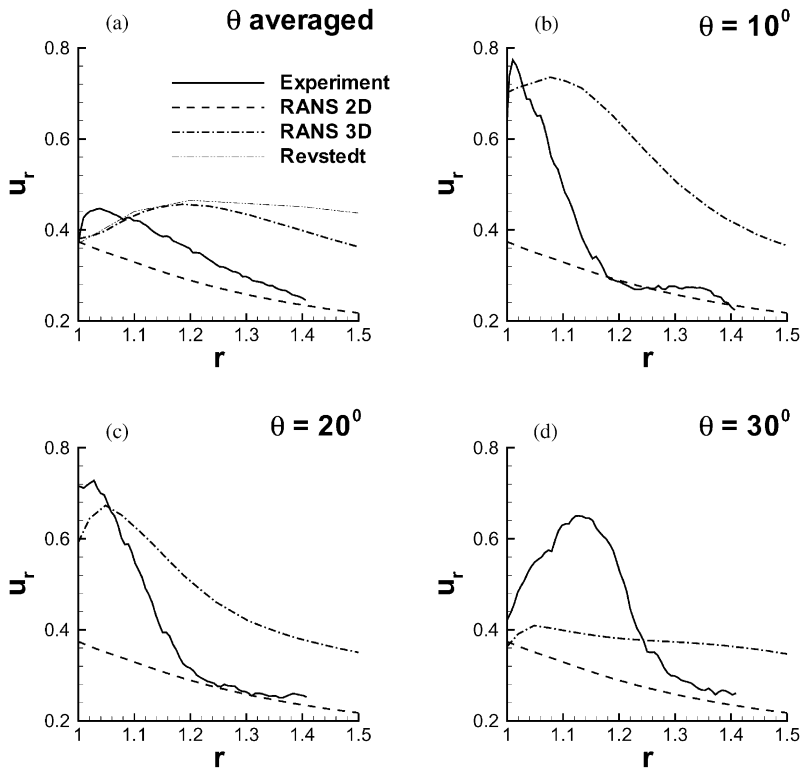


Fig. 16. Comparison of the radial velocity profile along the tank centerline at $z = 0$. The 3D results are compared with the experimental measurement and also with the 2D simulation and the results of Revstedt et al. (1998). (a) $\theta$-averaged profile, (b) $\theta = 10^{\circ}$, (c) $20^{\circ}$ and (d) $30^{\circ}$.

boundary condition, which incorporates the effect of the tip vortex pair, even Reynolds-averaged simulation is able to capture the effect of tip vortices in the interior. Fig. 16 also shows the computational results of Revstedt et al. (1998). Their geometry and operating conditions are somewhat different, and in order to facilitate comparison their result has been scaled to match the velocity at $r = 1$. Very good comparison between Revstedt et al's. (1998) data and the 3D simulation can be seen, but neither agrees very well with the experiments.

The influence of the tip vortices can be more clearly seen in Figs. 16b–d where $u_r$ is plotted against $r$ at three different azimuthal locations ($\theta = 10^{\circ}, 20^{\circ}$ and $30^{\circ}$) for the 3D simulation. The corresponding experimental measurements and the $\theta$-independent result of the 2D simulation are also plotted. The influence of the tip vortices is most dominant around $\theta = 20^{\circ}$. As the strength of the tip vortex pair decays for larger angles, their influence on the radial velocity also diminishes. One significant difference between the 3D simulation and the experimental data is that the experimental result falls off from the peak faster than the simulation. This difference can be traced back to the fact that while the experimental result showed that the jet centerline oscillated about $z = 0$ at the exit of the impeller, the computations with a time-averaged mean boundary condition ignore this oscillation. As a result, the mean spreading rate of the jet is faster in the case of the experiment, resulting in a faster drop-off of the centerline velocity. Thus, it appears that a time-dependent boundary condition at the exit of the impeller is required in order to obtain better comparison with the experimental data. Another difference between the experimental data and the computation is that the peak radial velocity in the case of the experiment falls off faster with increasing $\theta$. While at $10^{\circ}$ and $20^{\circ}$ the peak radial velocity obtained in the 3D computation compared reasonably with the experimental measurement, at $30^{\circ}$ the computational peak is significantly lower than the experimental peak. This is because the strength of the tip vortices is not properly maintained in the Reynolds-averaged simulation. As a result, the tip vortex decays faster, and the peak radial velocity induced by the tip vortex pair falls faster. This indicates that a time-dependent simulation, such as large eddy simulation or unsteady Reynolds-averaged simulation, with the theoretical model as the boundary condition may be able to perform even better than RANS.

Fig. 17 shows the velocity vector plot from the 3D simulation at various azimuthal locations in the region close to the impeller swept volume. The tip vortices can be seen clearly from $0^{\circ}$ to about $20^{\circ}$. They persist for $\theta > 20^{\circ}$ as well, but they are too weak to be directly identified from the total velocity field. They can be isolated and extracted by subtracting the jet component. Interestingly the tip vortex can be seen also at $\theta = 0^{\circ}$. In real-

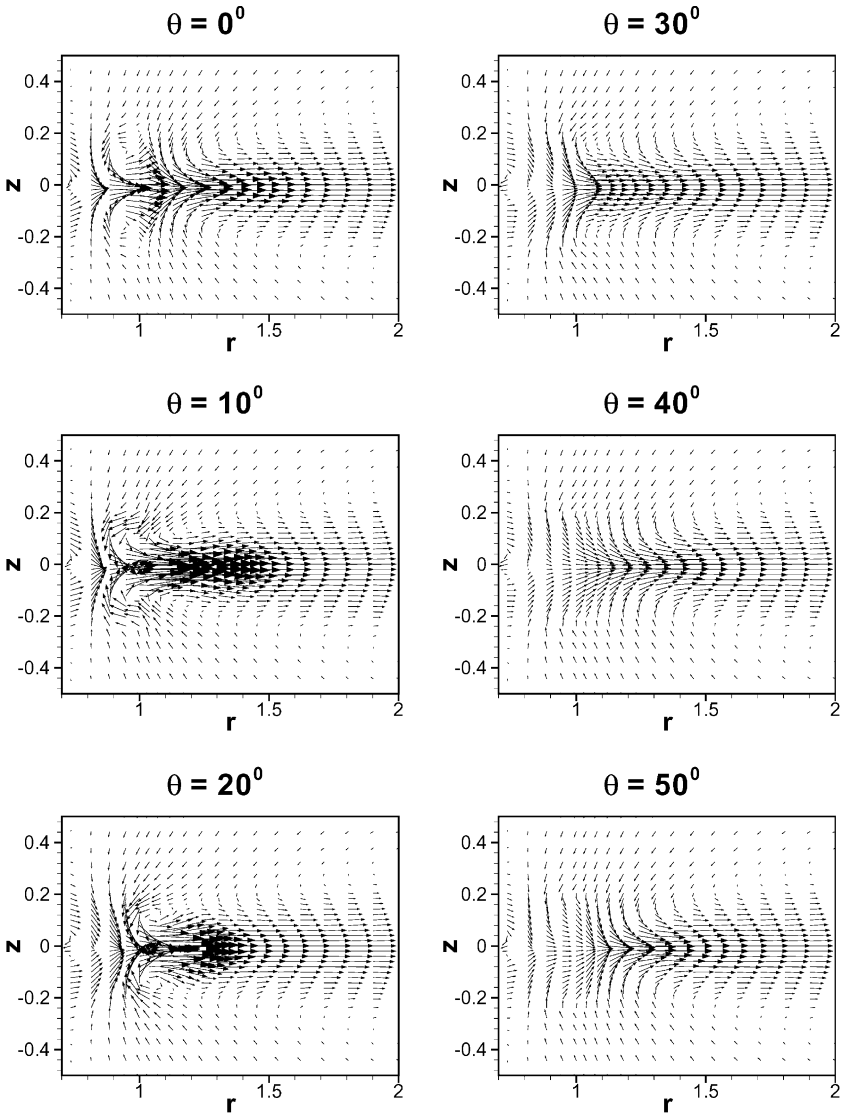


Fig. 17. Velocity vector plot from the three-dimensional simulation at various azimuthal locations in the region close to the impeller swept volume: (a) $\theta = 0^\circ$, (b) $10^\circ$, (c) $20^\circ$, (d) $30^\circ$, (e) $40^\circ$ and (f) $50^\circ$.

ity, due to the presence of the impeller blade the axis of the tip vortex pair turns sharply and runs parallel to the blade as shown schematically in Fig. 1. In the computation, the presence of the impeller blade is not directly accounted for; only its influence is modeled as the inlet velocity field. As a result the tip vortex pair can be seen to extend even backwards up to $\theta = 0^\circ$.

Fig. 18a shows the in-plane velocity vector on a $\theta$–$z$ plane located at $r = 1.1$ obtained from the 3D simulation. The corresponding out-of-plane radial velocity is shown in Fig. 18b. The vector plots clearly show the presence of tip vortices extending into the tank in the 3D Reynolds-averaged simulation. They have an influence on the radial velocity as well. The radial velocity can be observed to increase since the tip vortices cut the constant $r$ plane at an angle. With increasing radial location the azimuthal and the axial location of the vortex centers change, describing the vortex trajectory as captured by the simulation. The tip vortex influence decays more rapidly in case of the Reynolds-averaged simulations. A time-dependent simulation is necessary in order to recover more physics in the simulation.

## 5. Conclusion

Two sets of experiments have been performed to quantify flow induced by a six-blade Rushton turbine in a stirred tank without baffles. The first set of PIV measurements was taken on six different $r$–$z$ planes phase locked at $0^\circ, 10^\circ, 20^\circ, 30^\circ, 40^\circ$ and $50^\circ$ with respect to the blade location. The second set of measurements employed a

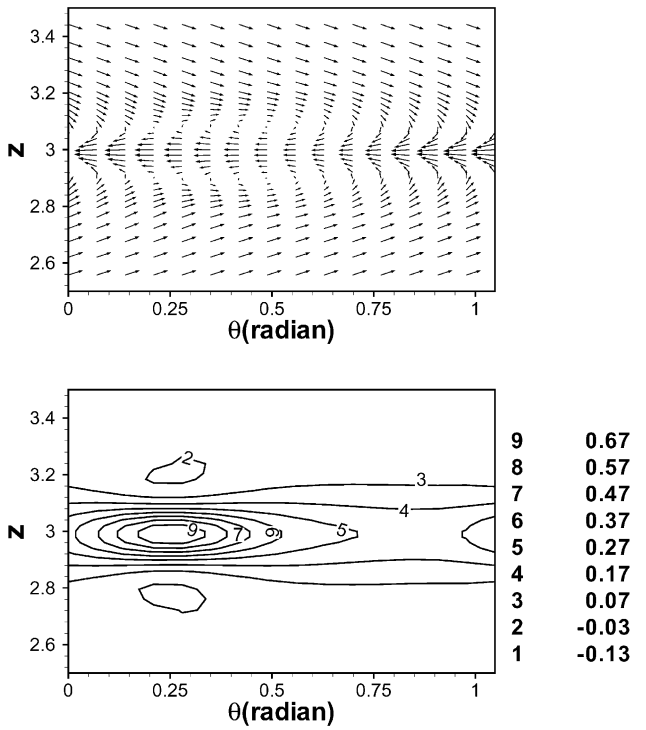


Fig. 18. The in-plane velocity vector on a $\theta$–$z$ plane located at $r = 1.1$ obtained from the three-dimensional simulation.

novel arrangement such that stereoscopic PIV measurements could be obtained on a curved $\theta$–$z$ plane whose radial location is just outside the impeller blade tip radius.

The experimental measurements are used to construct a velocity boundary condition for numerical simulation. The computation is limited to the region outside the impeller swept volume and the impeller-induced flow is applied as the inlet boundary condition. The impeller-induced flow, as measured in the experiments, is quite complex. It has all three components of velocity, dependent on all three coordinate directions. In this sense the velocity boundary condition significantly extends earlier attempts wherein the impeller-induced flow was modeled as a jet flow, and the $\theta$-dependence of the flow was typically ignored. It must be emphasized that owing to the complex nature of the 3D impeller-induced flow a curve fit through the experimental data, is not straightforward.

We have taken a physics-based approach to describe the impeller-induced flow. Experimental measurements show that the flow in the vicinity of the impeller is decomposed into a circumferential flow, a jet flow, and pairs of tip vortices for each impeller blade. Simple model for each of the flow component is constructed to produce an overall model for the impeller-induced flow. The circumferential flow is characterized by its radial profile and is independent of both $\theta$ and $z$; the jet flow is characterized by its strength, width and virtual origin; and the tip vortices are characterized by their trajectory, strength and thickness. The model allows for a compact characterization of the impeller-induced flow with a small number of parameters. Comparison of the model with the measurements both on the $r$–$z$ and $\theta$–$z$ planes shows that the model provides an adequate description of the impeller-induced flow.

Scaling is a central issue in the design of stirred tank reactors. In particular, scaling of the impeller-induced flow with impeller geometry and operating condition has been very challenging. The theoretical model provides a framework to examine complex scaling of the impeller-induced flow. The scaling of the circumferential flow, jet and tip vortex components of the impeller-induced flow has been obtained over a narrow range of impeller rpm. The result shows that each component might follow a simple scaling law, but the overall impeller-induced flow can exhibit complex scaling, since the scaling of each of the component is different.

The theoretical model presented here is simple and provides ample opportunity for further improvement, whereby additional complex physics associated with the impeller-induced flow can be built into the model. The instantaneous realizations show that the impeller-induced flow, even in the vicinity of the swept volume, is time dependent. The time dependence can be introduced into the model in several different ways. Parametrization implicit in the model allows for time-dependent strength and width for the different flow components. The amplitude and frequency of time dependence can be varied to better match the experimental observation. A closer look at the instantaneous PIV measurements on the $r$–$z$ plane reveals that the nature of the time dependence is such that the centerline of the jet flow out of the impeller is not strictly aligned with the radial direction. The direction of the jet flow appears to oscillate up and down. Furthermore, in the instantaneous realizations the tip vortices which are nominally located above and below $z = 0$ plane are not perfectly symmetric. Their relative strength appears to vary over time.

2D and 3D Reynolds-averaged Navier–Stokes simulations were performed using the commercial code FLUENT® with the model of the impeller-induced flow as the boundary condition. The 3D simulation included the effect of tip vortices, whereas the $\theta$-average implicit in the 2D simulation eliminates the details of the tip vortices. As a result the 3D results are in better qualitative agreement with the experiments. Even so, the results of Reynolds-averaged simulations quantitatively differ from experimental measurement. Dynamics of the different scales of motion needs to be accounted for through a unsteady RANS or direct or large eddy simulation for further improvement in prediction. Nevertheless, the improvement of the present model over the conventional boundary condition is evident in the computational results.

## Acknowledgements

HSY, SB and MYH were partly supported by a grant from the Dow Chemical Company. KVS was supported by Mavis Fellowship and National Science Foundation Fellowship. DFH was supported by funding from the Leonard C. and Mary Hoeft Endowed Chair of Engineering.

## References

Calabrese, R. V., & Stoots, C. M. (1989). Flow in the impeller region of a stirred tank. *Chemical Engineering Progress*, *85*, 43–50.

Desouza, A., & Pike, R. W. (1972). Fluid dynamics and flow patterns in stirred tanks with a turbine impeller. *Canadian Journal of Chemical Engineering*, *50*, 15.

Eggels, J. M. G. (1996). Direct and large eddy simulation of turbulent fluid flow using the lattice-Boltzmann scheme. *International Journal of Heat Fluid Flow*, *17*, 307–323.

Hill, D. F., Sharp, K. V., & Adrian, R. J. (2000). Stereoscopic particle image velocimetry measurements of the flow around a rushton turbine. *Experimental Fluids*, *29*, 478–485.

Ju, S. Y., Mulvahill, T. M., & Pike, R. W. (1990). Three-dimensional turbulent flow in agitated vessels with a nonisotropic viscosity turbulent model. *Canadian Journal of Chemical Engineering*, *68*, 3.

Kolar, V., Filip, P., & Curev, A. G. (1982). The swirling radial jet. *Applied Science Research*, *39*, 329–335.

Kolar, V., Filip, P., & Curev, A. G. (1984). Hydrodynamics of a radially discharging impeller stream in agitated vessels. *Chemical Engineering and Communication*, *27*, 313–326.

Kresta, S. M., & Wood, P. E. (1991). Prediction of the three-dimensional turbulent flow in stirred tanks. *A.I.Ch.E. Journal*, *37*, 448–460.

Lee, K. C., Ng, K., & Yianneskis, M. (1996). Sliding mesh predictions of the flow around Rushton impeller. *ICHEME Symposium Series*, *140*, 47–58.

Luo, J. V., Gosman, A. D., Issa, R. I., Middleton, J. C., & Fitzgerald, M. K. (1993). Full flowfield computation of mixing in baffled stirred reactors. In *proceedings of the IChemE research event*, Birmingham, UK (pp. 657–659).

Nielsen, H. J. (1958). Ph.D. thesis, Illinois Institute of Technology, Chicago.

Pericleous, K. A., & Patel, M. K. (1987). The source-sink approach in the modeling of stirred reactors. *PhysioChemical Hydrodynamics*, *9*, 279–297.

Placek, J., & Tavlarides, L. L. (1985). Turbulent flow in stirred tanks. I: Turbulent flow in the turbine impeller region. *A.I.Ch.E. Journal*, *31*, 1113.

Ranade, V. V., Joshi, J. B., & Marathe, A. G. (1989). Flow generated by pitched blade turbines. II: Simulation using k–e model. *Chemical Engineering and Communication*, *81*, 225–248.

Rao, M. A., & Brodkey, R. S. (1972). Continuous flow stirred tank turbulence parameters in the impeller stream. *Chemical Engineering Science*, *27*, 137–156.

Revstedt, J., Fuchs, L., & Tragardh, C. (1998). Large eddy simulation of the turbulent flow in a stirred reactor. *Chemical Engineering Science*, *53*, 4041–4053.

Saffman, P. G. (1992). *Vortex dynamics*. Cambridge: Cambridge University Press.

Schwarz, W. H. (1963). The radial free jet. *Chemical Engineering Science*, *18*, 779.

Sharp, K. V., Kim, K. S., & Adrian, R. J. (1998). A study of vorticity and dissipation around a Rushton turbine using particle image velocimetry. *Proceedings of the Ninth international symposium on applications lasers to fluid mechanics*, Lisbon, July 13–16 (pp. 14.1.1-10).

Van't Riet, K., & Smith, J. M. (1975). The trailing vortex system produced by Rushton turbine agitators. *Chemical Engineering Science*, *30*, 1093.

Yianneskis, M., Popiolek, Z., & Whitelaw, J. H. (1987). An experimental study of the steady and unsteady flow characteristics of stirred reactors. *Journal of Fluid Mechanics*, *175*, 537.